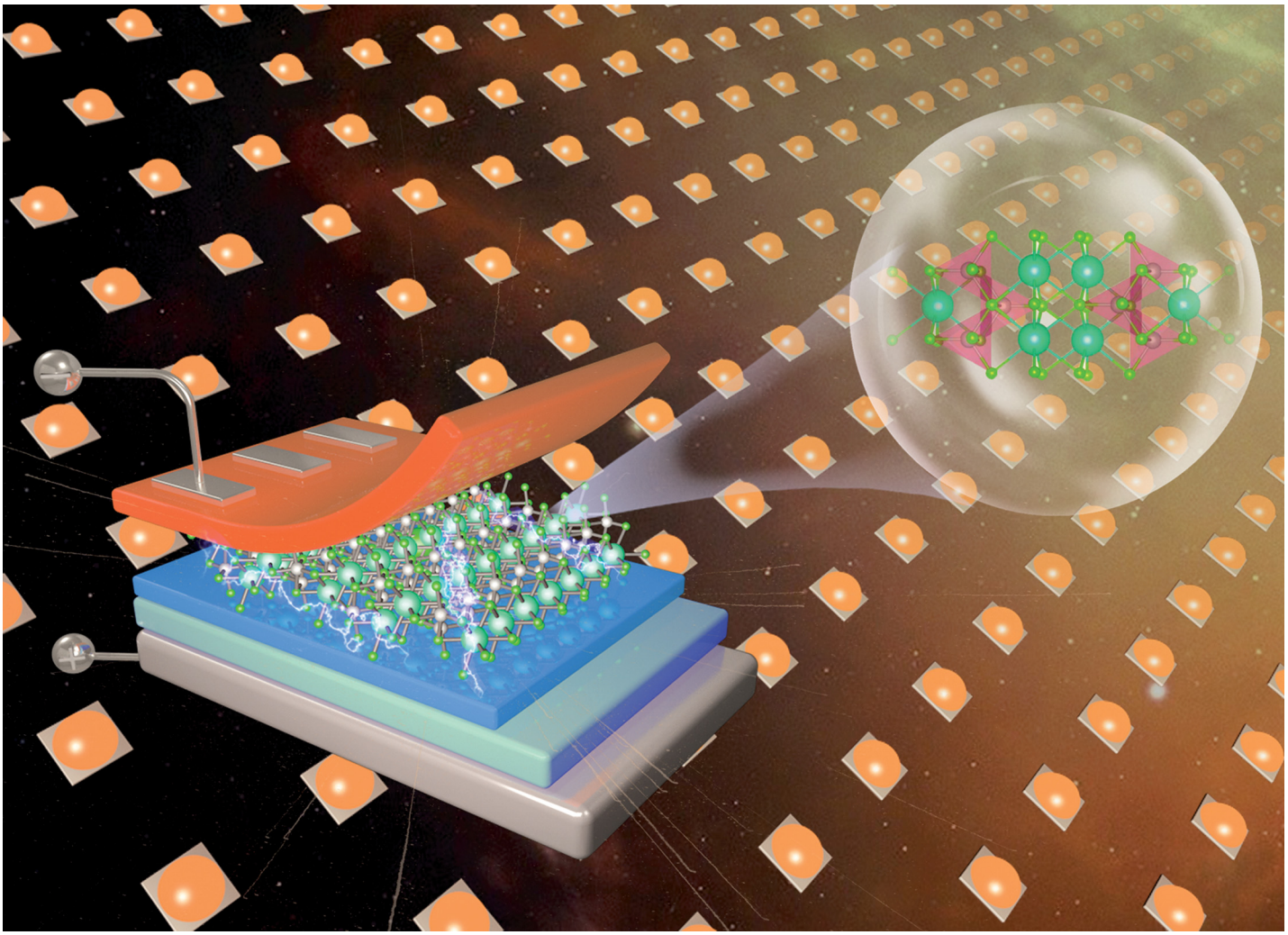

Showcasing research from Professor Feng Liu's laboratory, Institute of Frontier and Interdisciplinary Science, Shandong University, Qingdao, P. R. China.

Colloidal synthesis of size-confined $CsAgCl_2$ nanocrystals: implications for electroluminescence applications

A facile solution-based route to $CsAgCl_2$ nanocrystals was devised. Sb^{3+} dopant was found to have the ability to control particle size of the nanocrystals in the quantum confinement regime, as well as to enhance their PLQYs from 17% to 38%. LEDs fabricated with these nano-emitters exhibit fascinating warm white-light emission, which opens up new avenues to develop single-component warm white LEDs.

As featured in:

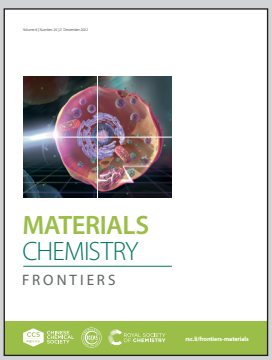

See Junke Jiang, Feng Liu *et al.*, *Mater. Chem. Front.*, 2022, **6**, 3669.

ROYAL SOCIETY OF CHEMISTRY

rsc.li/frontiers-materials

Registered charity number: 207890

MATERIALS CHEMISTRY FRONTIERS

RESEARCH ARTICLE

View Article Online
View Journal | View Issue

Cite this: *Mater. Chem. Front.*, 2022, **6**, 3669

Colloidal synthesis of size-confined $CsAgCl_2$ nanocrystals: implications for electroluminescence applications†

Sujun Ji,[a] Xuan Meng,[a] Xiaochen Wang,[a] Tianxin Bai,[a] Ruiling Zhang,[a] Bin Yang,[b] Keli Han, ‡[ab] Junke Jiang §*[c] and Feng Liu*[a]

Because of their non-toxic properties and similar ionic radius to that of Pb^{2+}, silver ion (Ag^+)-containing perovskite derivatives have become an important class of Pb-free alternatives that are competitive for a variety of optoelectronic applications. Although great success has been achieved in producing Ag^+-containing nanocrystals (NCs), such as $Cs_2AgInCl_6$ and $Cs_2AgBiCl_6$, colloidal synthesis of pure Ag-based emitters has remained challenging. Herein, we have devised a facile europium chloride ($EuCl_3$)-based route to $CsAgCl_2$ NCs with a tunable particle size and desirable warm white-light emission. To enhance the optical properties of $CsAgCl_2$, we further demonstrate a trace doping strategy with Sb^{3+}, which improves the quantum efficiency of the resulting NCs from 16% to 39%. Moreover, the addition of Sb^{3+} was found to significantly reduce the particle size of the $CsAgCl_2$ NCs from a few hundred nanometers to several nanometers as a result of the reduced surface energy, paving the way for the formation of emissive layers with a well-controlled thickness and improved uniformity. Prototype electroluminescence devices fabricated using these nano-emitters exhibit favorable warm white-light (or yellow) emission, which opens up new avenues to develop single-component warm white light-emitting diodes.

Received 29th September 2022,
Accepted 20th October 2022

DOI: 10.1039/d2qm00997h

rsc.li/frontiers-materials

Introduction

Lead (Pb)-free metal halide perovskites and their derivatives have drawn tremendous interest for many emerging applications because of their benefits of reduced toxicity and possibilities of broadband white-light emission, which is enabled by their self-trapped excitons (STEs).[1–5] Recently, these materials were extensively studied in the form of nanocrystals (NCs) and used as potential candidates for light-emitting diodes (LEDs) owing to their high photoluminescence quantum yields (PLQYs) and high compatibility with low-cost solution-based processes. The merits of rendering the emitters in the form of NCs include the versatile colloidal syntheses, which allow a facile surface modification of the semiconductors *via* organic ligands and hence enable a higher PLQY. Moreover, because of the excellent homogeneity and dispersibility of NCs in colloidal solution, thin films deposited from NCs usually have a uniform morphology and a pinhole-free surface, which benefit the fabrication of high-efficiency devices.[6,7] For example, electrically driven deep-blue LEDs based on $Cs_3Cu_2I_5$ NCs demonstrated high external quantum efficiency (EQE) that reached over 1%, comparable with those of the best-performing Pb-halide perovskites.[8] In addition, LEDs fabricated with violet emissive $Cs_3Sb_2Br_9$ NCs showed a decent EQE of 0.2% and an excellent working stability, making them a strong candidate for the preparation of environment-friendly and stable violet LEDs.[9]

Apart from Cu^+ and Sb^{3+}, the non-toxic silver (Ag) element has also been widely investigated for developing Pb-free luminescent materials because of its similar ionic radius to that of Pb^{2+} and a relatively higher air stability than that of Cu^+. More recently, Qu *et al.* demonstrated warm white LEDs using $CsAgIn_{0.9}Bi_{0.1}Cl_6$ NCs, which exhibited an impressive maximum luminance of 158 cd m^{-2}, an EQE of 0.08%, and a high color-rendering index of 94.5.[10] It is worth mentioning that some pure Ag-based metal halides, such as zero-dimensional

[a] *Institute of Molecular Sciences and Engineering, Institute of Frontier and Interdisciplinary Science, Shandong University, Qingdao 266237, P. R. China. E-mail: fenglau189@sdu.edu.cn*
[b] *State Key Laboratory of Molecular Reaction Dynamics, Dalian Institute of Chemical Physics, Chinese Academy of Science, Dalian 116023, P. R. China*
[c] *Materials Simulation and Modelling, Department of Applied Physics, and Center for Computational Energy Research, Department of Applied Physics, Eindhoven University of Technology, Eindhoven 5600 MB, The Netherlands. E-mail: j.jiang1@tue.nl*

† Electronic supplementary information (ESI) available: Experimental details, DFT calculations, TEM images, SEM-EDS maps, XPS spectra, XRD patterns, quantitative analysis results, PL and EL spectra, and energy band diagram of the LED devices. See DOI: https://doi.org/10.1039/d2qm00997h

‡ Deceased 17 March 2022.

§ Present address: Univ Rennes, ENSCR, CNRS, ISCR-UMR 6226, F-35000 Rennes, France.

(0D) orthorhombic-phase $CsAgCl_2$, also possess the broadband warm white-light emitting properties, making it unnecessary to use those rare earth elements, *e.g.*, In^{3+}, in the fabrication of warm white LEDs.[11] However, unlike the aforementioned Cu-, Sb-based halides and Ag–In (–Bi)-based double perovskites, which readily crystallize in the form of NCs, the pure Ag-based crystals exist mainly in the form of bulks or powders, whose PLQYs are typically lower than 20%.[11,12] Moreover, difficulties in assembling these bulks or powders into functional thin films have also seriously hampered the optimal utilization of their potential in optoelectronics. As such, it is highly desirable to establish an effective synthetic route to high-quality pure Ag-based emitters of nano-scale size featuring high colloidal stability and good film-forming ability.

Herein, we report an unconventional yet highly effective route to nanosized $CsAgCl_2$, which readily forms a stable colloidal suspension with a tunable particle size and broadband light emission covering the entire visible spectral region from 450 to 900 nm. The main modifications that we made were (i) the use of a novel halide source, $EuCl_3$, which exhibits favorable thermodynamics for the formation of $CsAgCl_2$ metal halide without incorporation of the Eu^{3+} ions and (ii) trace doping with Sb^{3+}, which reduces the surface energy of $CsAgCl_2$, enabling the formation of size-confined nanoparticles as well as significantly improved PLQY. Thanks to the high colloidal stability and good film-forming ability of the resulting NCs, we are allowed to fabricate electrically driven LEDs using a low-cost solution-based method, which show bright warm white-light emission with a maximum luminance of 9.6 cd m^{-2} and an EQE of 0.02%. These results show that the pure Ag-based metal halides hold great potential for use in single-component low-cost and non-toxic light-emitting devices.

Results and discussion

Synthesis of warm white light-emissive $CsAgCl_2$ metal halide NCs from cesium acetate (CsOAc), silver acetate (AgOAc), and chlorotrimethylsilane (TMSCl) following traditional methods for the $Cs_2AgBiCl_6$ perovskite NCs[13,14] was unsuccessful and led to non-dispersible products, which mainly consisted of rod-shaped crystals whose lateral length reached over 500 nm (see Fig. S1a, ESI†). Although these non-dispersible large particles contain the same Cs, Ag, and Cl elements, as evidenced by energy-dispersive X-ray spectroscopy (EDS) mapping analysis (Fig. S1b, ESI†), X-ray diffraction (XRD) measurements suggest that they do not form orthorhombic-phase $CsAgCl_2$ (Fig. S1c, ESI†). This is corroborated by measuring their optical properties, where we see no PL response under 254 nm UV irradiation (Fig. S1d, ESI†), in stark contrast to that of orthorhombic-phase $CsAgCl_2$, which exhibits strong light emission covering the entire visible spectral region from 450 to 900 nm.[12]

In order to prevent such an undesirable reaction and to enable a better control over the morphology of the resulting nanocrystalline materials, we turned to optimize the synthesis parameters by using an alternative halide source because halide precursors play an important role in influencing the growth kinetics of the metal halide NCs and may dictate the type of compounds that can be formed.[15–17] Herein, nine different types of halide salts were investigated including $SbCl_3$, YCl_3, $TbCl_3$, $EuCl_3$, $InCl_3$, $CeCl_3$, $ErCl_3$, $GeCl_4$, and $ZnCl_2$. These inorganic halide compounds were first dissolved in a coordinating solvent trioctylphosphine oxide (TOPO) and then injected into a CsOAc and AgOAc precursor solution at 170 °C, which contained oleic acid (OA) and oleylamine (OAm) (more experimental details can be found in the ESI†). Despite the same amount of Cl^- ions provided by these different types of halide sources, the XRD results evidence that only $EuCl_3$ could produce orthorhombic-phase $CsAgCl_2$, without any traces of secondary phases (Fig. 1a and Fig. S2, ESI†). All these observations point to the fact that varying Cl precursors has led to different growth kinetics for the $CsAgCl_2$ NCs, which we consider to have resulted from the different reactivities of the Cl-containing precursors toward dechlorination because according to the Arrhenius equation, the crystallization kinetics of the NCs is largely dependent on the activation energy of the used precursors.[18] To better illustrate the chemical difference between these halide donors, we analyzed quantitatively their metal–halide bond strength using density functional theory (DFT) simulations. The calculated bond energy increases in the order of $EuCl_3 < TbCl_3 < ErCl_3 < CeCl_3 < YCl_3 < SbCl_3 <$ TMSCl $< InCl_3 < GeCl_4 < ZnCl_2$ (see Table S1, ESI†), which indicates that $EuCl_3$ is the most reactive compound toward dechlorination, and due to the weak Eu–Cl bond in $EuCl_3$, we expect a low activation energy for Cl^- ion release by using $EuCl_3$. Difference in reactivities of the Cl precursors thus results in different growth kinetics of the metal halide NCs and finally dictates the type of these Cl-based compounds that can be formed.[19]

The $EuCl_3$-produced colloids can be readily dispersed in non-polar solvents with a high colloidal stability. The transmission electron microscopy (TEM) image (Fig. 1b) reveals their oval-like morphology with the particle size ranging from 200 to 300 nm. TEM-EDS elemental maps show that the Cs and Cl elements are homogeneously distributed throughout the sample while Ag tends to be localized in specific regions of the crystals (Fig. 1c). This can be due to the reduction of part of Ag^+ in NCs to Ag nanoparticles as observed under a high-energy electron beam of an electron microscope.[13,19] Similar results were observed when Pb perovskites were exposed to electron-beam irradiation in TEM measurement, which usually produces metallic Pb atoms.[20–22] To gain more accurate information about the element distribution in the NCs, scanning electron microscopy (SEM)-EDS which typically uses lower energy beams was performed. As expected, Cs, Ag, and Cl elements are now shown to be homogeneously distributed along the crystals (Fig. S3, ESI†), which supports the suggestion that $CsAgCl_2$ NCs could be unstable under high-energy electron beams.

When using a Eu-containing halide source precursor, it is important to ascertain whether the Eu element is present in the final NCs. To this end, chemical composition of the

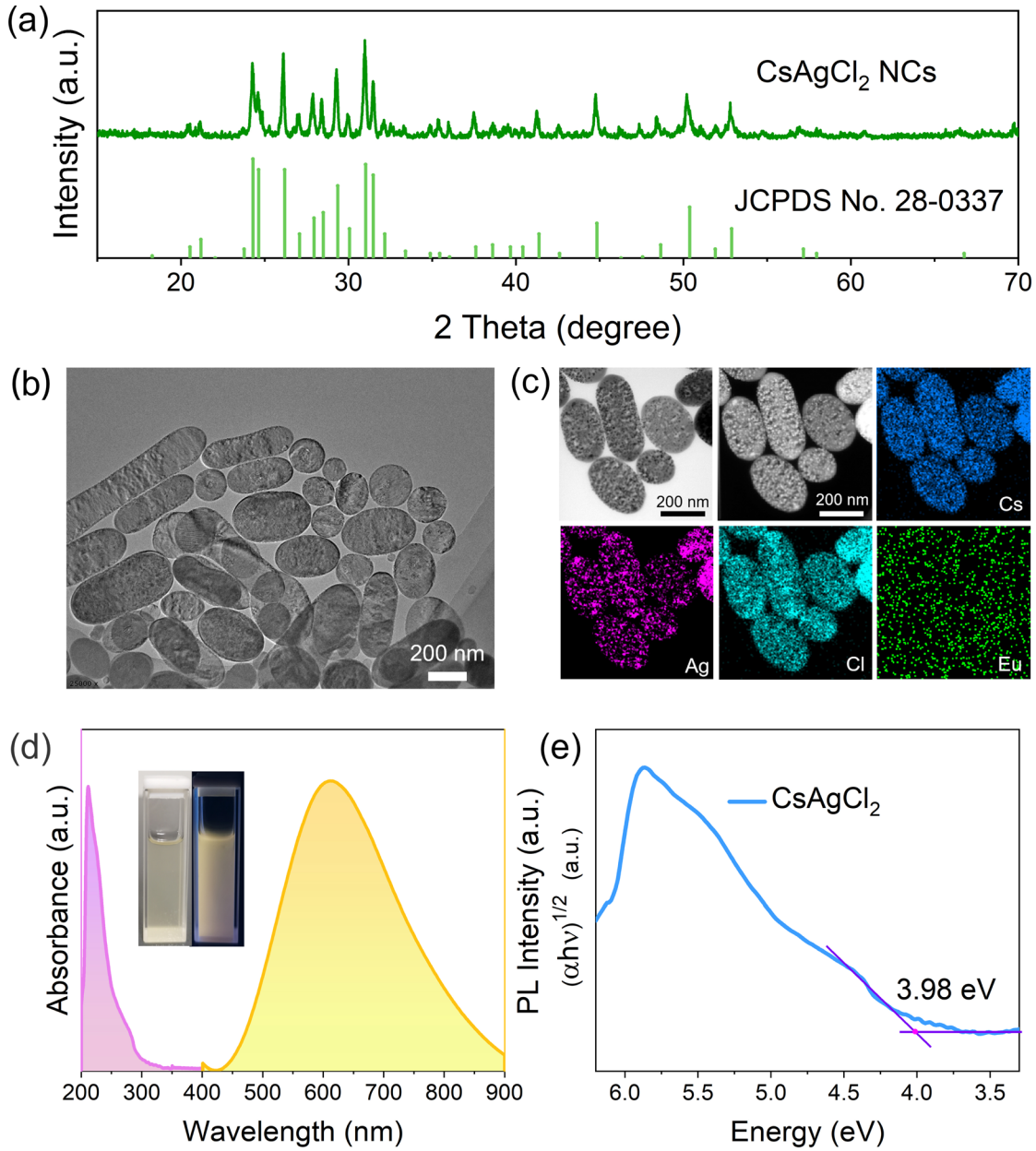

Fig. 1 (a) XRD pattern, (b) TEM images, (c) TEM-EDS microanalysis map, and (d) UV-vis absorption/PL spectra of the $EuCl_3$-prepared NCs. The vertical bars in Fig. 1a represent the position of the simulated diffraction peaks for the bulk orthorhombic-phase $CsAgCl_2$ (JCPDS No. 28-0337). The inset in Fig. 1d shows the picture of a typical NC solution taken under ambient light (left) and 254 nm UV light (right), respectively. (e) Tauc plot for determining the indirect band gap of $CsAgCl_2$ NCs.

$EuCl_3$-prepared samples was first evaluated by quantitative analysis using inductively coupled plasma-mass spectrometry (ICP-MS), which showed that the Eu element has a low concentration of $<0.01\%$. This is in accordance with the TEM-EDS results, where the Eu view window contains basically the background noise (Fig. 1c). Furthermore, when we had a close look at the XRD pattern of the resulting NCs prepared using $EuCl_3$ (see Fig. 1a), we found no noticeable peak shift with respect to the standard orthorhombic-phase $CsAgCl_2$, signifying that the lattice parameter of the $CsAgCl_2$ NCs remains unchanged. Based on these, we may safely conclude that the Eu element virtually does not exist in the lattice of the final products, *i.e.*, $EuCl_3$ possesses favorable thermodynamics for the formation of $CsAgCl_2$ but it does not deliver Eu^{3+} ions into the NC lattice. A similar result was reported using a germanium halide-based route to a variety of colloidal metal halides, where no sign of $Ge^{2+/4+}$ incorporation was found in the final NCs.[16,19]

To investigate the role of organic ligands in influencing the final products of $CsAgCl_2$, we conducted contrast synthesis by removing OAm from the starting solution, while keeping other parameters constant. Interestingly, it was found that in the absence of OAm, the solution mixture of OA and octadecene

itself can also dissolve Ag(OAc) and Cs(OAc), which should form Ag–oleate and Cs–oleate complexes, respectively. However, XRD measurement suggests that the final products are different from those synthesized with OAm (Fig. S4, ESI†). First, compared to the standard $CsAgCl_2$ XRD pattern, diffraction peaks at 28.4°, 30°, 38.6°, and 39.6° have disappeared from the new sample, which can be due to the change in the preferred crystallographic orientation. second, new diffraction peaks appear at 25.24°, 32.57°, 44°, 48.84°, 50.93°, and 59.5°, which are indicative of the formation of AgCl and some unknown byproducts in the sample. All these observations point to the fact that the removal of OAm has led to different growth kinetics for the $CsAgCl_2$ NCs. This can be explained as the growth of Ag-containing metal halide NCs is favorable on Ag nanoparticles that serve as seeds for nucleation, and according to the results of Levy *et al.*'s study, the addition of OAm will trigger the formation of Ag nanoparticles prior to injection of halide.[23] In this sense, OAm is indispensable, and plays a key role in synthesizing pure-phase $CsAgCl_2$ NC products.

Studying the photophysical properties of a luminescent material using UV-vis absorption and PL spectroscopy is of paramount importance for assessing its suitability for light-emitting applications. Fig. 1d shows that $CsAgCl_2$ NCs exhibit a broadband emission from 450 to 900 nm and have a large Stokes shift of 313 nm, which are typical features of STE emission.[11,12] The negligible overlap between their absorption and emission spectra is favorable to LEDs as one would expect minimum loss of light emission in thin films unlike excitonic or band edge emission. The inset in Fig. 1d presents a typical photograph of the prepared NC solution, which shows very stable warm white-light (or yellow) emission under 254 nm ultraviolet light. The indirect band gap of $CsAgCl_2$ NCs was determined to be ~3.98 eV according to the related Tauc plot (Fig. 1e), and is close to that previously reported for large-sized $CsAgCl_2$.[11,12] PL performance of the resulting NCs was further evaluated by measuring their PLQYs using a commercial Hamamatsu setup, which give a moderate value of 16% ± 1%. Considering the indirect band gap structure of $CsAgCl_2$, such PL performance is generally acceptable, especially when compared to those of widely investigated Ag/In-, Ag/Bi-based double perovskites, such as $Cs_2AgInCl_6$ and $Cs_2AgBiBr_6$, which typically yield PLQYs <1%.[24]

To better utilize the intrinsic warm white light-emitting properties of $CsAgCl_2$ NCs and to enhance their future prospects and potential in LED applications, we aim to further improve their PLQYs by metal doping, a common strategy which is typically employed in Pb-free halides for enhancing their PL performance.[25,26] Herein, we found that trace Sb^{3+} doping can significantly improve PLQY of the pristine NCs without affecting their spectral range and symmetry (see Fig. 2a and b) (experimental details about Sb^{3+} doping can be found in the ESI†). The direct evidence of the presence of the Sb element in $CsAgCl_2$ NCs was given by TEM-EDS mapping. Fig. 2c shows that unlike the Eu view window which again does not have the necessary signal-to-noise ratio to be considered processable, we see a clear distribution signal of the Sb element in the resulting NCs. Table S2 (ESI†) summarizes the actual content of Sb in the purified sample, determined by ICP-MS. The optimally doped NCs with ~1.0 mol% Sb^{3+} exhibit a PLQY of ~39%, more than a twofold increase with respect to that of the undoped one. To identify whether the enhanced PLQY comes from the additional emission from Sb^{3+} ions, the emission wavelength-dependent PL excitation (PLE) spectra and excitation wavelength-dependent PL spectra were acquired. It was found that both PLE and PL spectra exhibited identical shapes at various emission (from 450 to 750 nm) and excitation wavelengths (from 230 to 275 nm) (Fig. S5 and S6, ESI†), indicating that the enhanced broadband emission originates from the relaxation of the same excited states and rules out the possibility of ion luminescence from Sb^{3+} with different excited-state levels.[27] XRD measurements confirm that the original crystal structure of the Sb^{3+}-doped NCs is well retained with doping levels between 0 and ~1.0 mol% because neither the diffraction peaks shift nor other secondary phases can be observed (Fig. 2d). This, combined with the TEM-EDS mapping results, suggest that the Sb element is mainly located on the surface of the $CsAgCl_2$ NCs, leaving the inner lattice parameters intact. Besides, the optical absorption spectrum of the Sb-doped NCs exhibits nearly identical shapes and features to those of the pristine one, suggesting that the band gap remains unchanged (Fig. 2e). The inset shows the Tauc plot of the doped NCs, from which a similar band gap of 3.99 eV was extracted. However, with a further increase in the Sb^{3+} concentration (>1.0 mol%), the crystal structure of the resulting NCs undergoes a significant change with almost-complete disappearance of diffraction peaks at 26.1°, 30.9°, and 31.4°, accompanied by the appearance of new peaks at 21.5° and 30.6° (assignable to CsCl, indicated with stars). This observation points to a detrimental effect of the excessive Sb^{3+} ions on the nucleation and growth of $CsAgCl_2$ NCs, and also rationalizes the decline in PLQY when the Sb^{3+} doping concentration reaches over 1.0 mol%.

To better illustrate the enhanced PLQY with Sb^{3+} doping (<1.0 mol%), time-resolved PL (TRPL) measurement was further carried out. It was found that the PL decay curve of both the pristine and doped crystals can be fitted using a single-exponential function, indicating that no other radiative recombination channel is introduced with the Sb dopant (Fig. 2f). The time constant of the undoped NCs is determined to be about 2.28 μs, which is close to that of the bulk one,[12] while the PL lifetime of the Sb^{3+}-doped NCs is increased to 2.67 μs. This result points to an enhanced exciton lifetime after Sb doping, which helps to increase the population of STEs and thus enables a higher PLQY. Given that the Sb element is not incorporated into the $CsAgCl_2$ NC lattice, we attribute the improvement to some kind of surface modification that is rendered by Sb^{3+} ions.

To confirm whether Sb atoms exist on the surface of the $CsAgCl_2$ NCs and provide surface modification for improving their optical properties, an XPS study on the Sb-doped $CsAgCl_2$ NCs etched with Ar^+ was further carried out (etching rate: 0.25 nm s^{-1}, 10 s for each etching cycle). Fig. S7 (ESI†) shows the evolution of the Sb 3d XPS spectra with the etching cycle

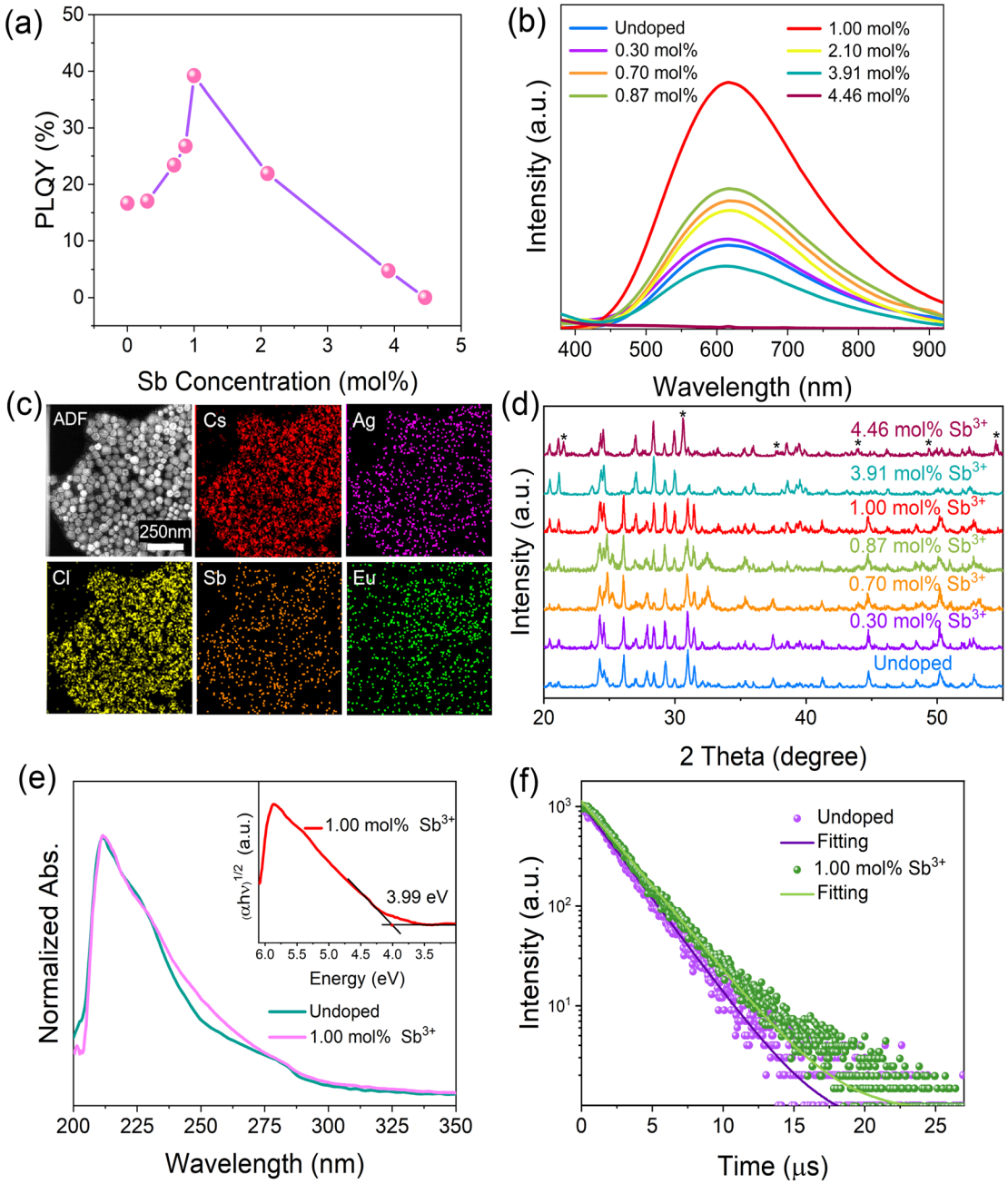

Fig. 2 (a) PLQY and (b) PL spectra of $CsAgCl_2$ NCs with different Sb^{3+} doping levels. (c) TEM-EDS elemental mapping results of 1.0 mol% Sb-doped NCs. (d) XRD patterns of 0–4.46 mol% Sb-doped NCs. (e) UV-vis absorption spectra (the inset shows the Tauc plot for the doped NCs) and (f) TRPL curves measured for the undoped and 1.0 mol% Sb-doped NCs at 300 K, monitoring the same emission peak at 625 nm.

and Fig. 3a shows the corresponding atomic concentration of the constituting elements. One can see a sharp decrease in the concentration with etching time for Sb, whereas for Cs/Ag/Cl the change in concentration is almost negligible. The behavior of the Cs/Ag/Cl/Sb atomic concentration during ion bombardment supports the suggestion concerning the surface location of Sb that can help explain the improvement in PLQY. The high-resolution TEM (HRTEM) technique is used to further visually verify the presence of Sb on the surface of $CsAgCl_2$ NCs. It is evident from Fig. 3b that the resulting NCs exhibit a well-defined core/shell structure consisting of a perfect crystalline core (interplanar spacing ~0.34 nm) surrounded by a surface shell (interplanar spacing ~0.29 nm). The surface shell presumably consists of Cs–Sb–Cl, Cs–Ag–Sb–Cl, or Sb–Cl, and acts as a passivation layer and hence eliminates surface defects for $CsAgCl_2$ NCs. As will be shown later, the trace amount of Sb^{3+} ions has also led to a significant change in the morphology of the $CsAgCl_2$ NCs. By fitting and comparing the temperature-dependent integrated PL intensity, we next examined the influence of Sb doping on exciton thermal activation energy

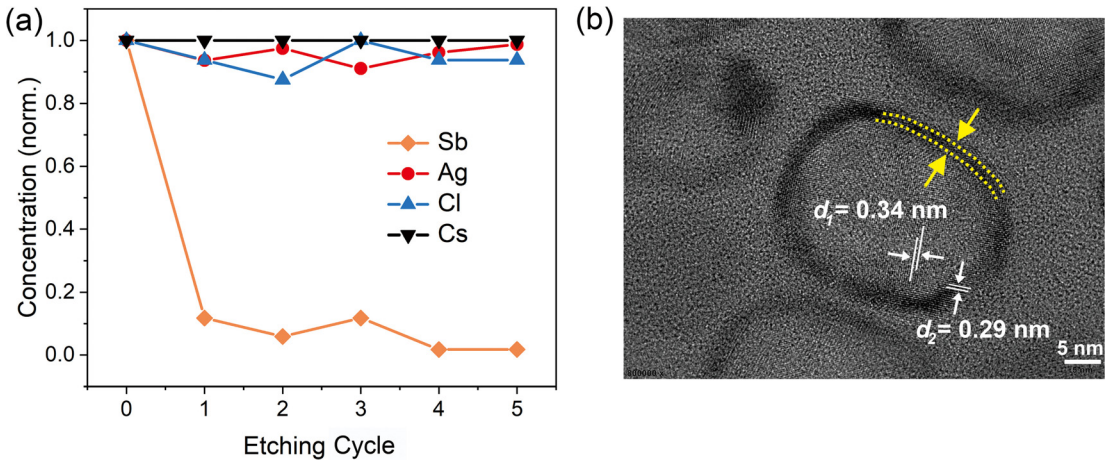

Fig. 3 (a) Normalized atomic concentration of the constituting elements as a function of etching cycle. (b) HRTEM image of the 1% Sb-doped $CsAgCl_2$ NCs.

(E_a) of the NCs, which is conducive to materials' radiative recombination processes. Fig. S8 (ESI†) presents the integrated PL intensity for both samples as a function of inverse temperature, which can be fitted by using the following Arrhenius equation:

$$I(T) = \frac{I_0}{1 + A\exp\left(\frac{-E_a}{k_B T}\right)} \quad (1)$$

where $I(T)$ is the integrated PL intensity at T, A is a constant, and k_B is the Boltzmann constant. It was found that the pristine $CsAgCl_2$ NCs possess an E_a of 132.1 meV, while an Sb-doped sample has an E_a value of 188.9 meV. The enhanced thermal activation energy will also contribute to a higher PLQY because it helps excitons to be localized at ambient temperature for efficient bound emission.[28]

Since Sb^{3+} ions tend to dope the surface region of $CsAgCl_2$, we therefore investigated the influence of Sb doping on the surface morphology of the resulting NCs. Fig. 4a–e present the TEM images of $CsAgCl_2$ NCs with a continuous change in the Sb^{3+} concentration, where we see a rapid decrease in the size from 258 to 28 nm. In Fig. 4e, we found some irregular voids in the measured NCs, which we attribute to the interactions of the $CsAgCl_2$ nanoparticles with the electron beam (beam damage) during TEM measurement. Yet another possible mechanism for the formation of voids could be associated with the nanoscale Kirkendall effect because metallic Ag nanoparticles would probably exist in a cation solution prior to

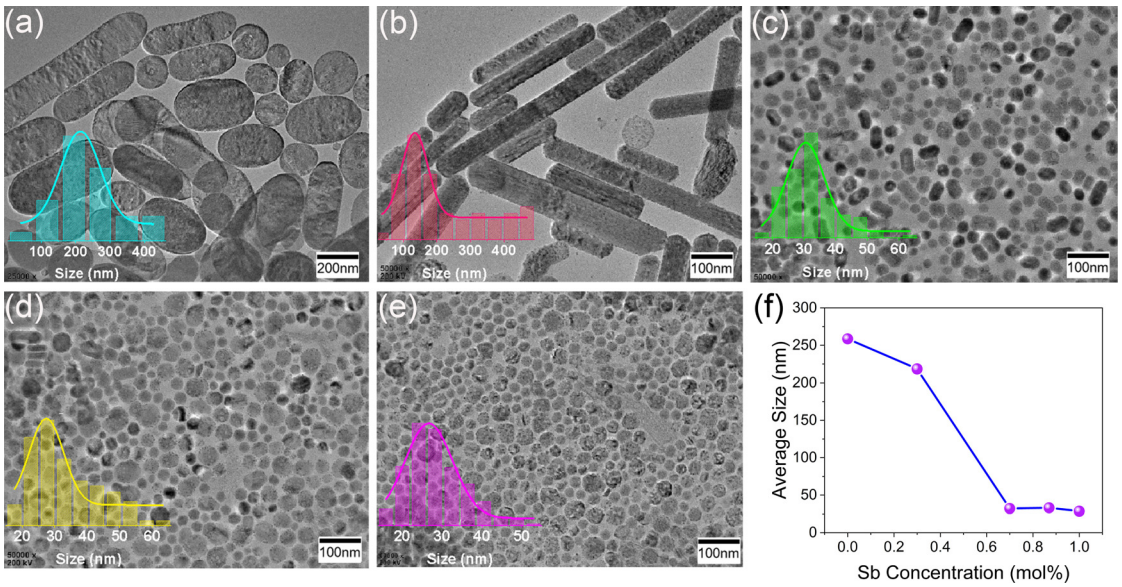

Fig. 4 TEM images of $CsAgCl_2$ NCs prepared with different Sb^{3+} doping levels. (a) 0 mol%, (b) 0.3 mol%, (c) 0.70 mol%, (d) 0.87 mol%, and (e) 1.00 mol%. (f) Particle size of the $CsAgCl_2$ NCs as a function of Sb^{3+} doping concentration.

injection of halide, and $CsAgCl_2$ NCs formed subsequently on Ag nanoparticles through the reaction with Cl and Cs atoms, which have different diffusivities.[23,29] Fig. 4f summarizes the particle size of the $CsAgCl_2$ NCs at different Sb^{3+} doping concentrations. In the absence of more complete data, we cannot state with certainty the nature of the decreased particle size observed in these Sb-doped $CsAgCl_2$ NCs; however, the possible change in the surface energy of the particles by Sb^{3+} doping appears to be a reasonable working hypothesis, see discussion 1 in the ESI.†

The broadband warm white-light emission, along with the small-size properties of these Sb^{3+}-doped NCs, render them highly attractive for use in singe-component warm white LEDs. For the demonstration, prototype electrically driven LEDs were first prepared using the most basic structure: indium tin oxide (ITO)/poly(3,4-ethylenedioxythiophene):poly(styrene sulfonate) (PEDOT:PSS)/NC film/2,2′,2″(1,3,5-benzenetriyl)tris-(1-phenyl-1*H*-benzimidazole) (TBPi)/LiF/Al on quartz (active area: 0.36 cm^2), shown schematically in Fig. 5a, along with the band alignment in Fig. 4b (experimental details can be seen in the ESI†). Note that the valence band maximum of the NCs is determined according to a previous report on $CsAgCl_2$ microcrystals.[11] Video 1 (ESI†) shows the real-time measurement of a typical LED device with voltage scanning. Excitingly, as the applied voltage increases, a bright warm white-light (or yellow) emission was seen with the naked eye, indicating that carriers are well confined in the NC layers and the recombination zone is mainly located at NCs. To our knowledge, this represents the first successful demonstration of electroluminescence (EL) from this kind of pure Ag-based metal halide. The inset of Fig. 5b shows a digital photograph of a uniform warm-white light from our NC LEDs driven by a 14 V bias. It should be noted, however, that such a device architecture cannot generate efficient EL, and due to the low luminous intensity, the EL spectra of these devices cannot be displayed. We consider it possible given the extremely low valence-band energy level of $CsAgCl_2$, which lies ~2.8 eV below that of PEDOT:PSS. Such a large energy barrier between the hole injection layer and the emissive layer would bring difficulties in hole injection, and hence deteriorate the EL performance. To increase the electrical parameters of the $CsAgCl_2$-based LEDs, a hole injection buffer layer, poly(9,9-dioctylfluorene-*alt*-*N*-(4-butylphenyl)-diphenylamine) (TFB), which is frequently used in previous quantum dot and perovskite LEDs, was further introduced between PEDOT:PSS and NCs because it allows a better band alignment which is favorable for hole transport (energy band diagram of the LED devices with the use of TFB is presented in Fig. S9, ESI†).[30–32] Fig. 5c shows a typical cross-sectional SEM image of the TFB-incorporated LEDs, where all device layers can be clearly identified. As expected, compared to the pure PEDOT:PSS-based LEDs, the TFB-incorporated LEDs exhibit brighter warm white-light emission. Fig. 5d presents the EL spectra of the LEDs under different applied biases with the inset showing bright emission from the device. As the applied voltage increases, a broadband EL signal starts to emerge with a peak at 628 nm and a bandwidth (full width at half-maximum, FWHM) of ~240 nm, which has a Commission Internationale de l'Eclairage (CIE) color coordinate of (0.42,0.41) and a correlated color temperature of around 3500 K in the warm white region (Fig. 5e). Such an emission characteristic is consistent with the PL properties of $CsAgCl_2$ NCs. Besides, the shape of the EL spectrum does not change in response to different applied voltages, indicating that the emission center is still mainly located on the NC layers. Fig. 5f presents the current–voltage–luminance (*I*–*V*–*L*) characteristics of the device. The LED turns on at a voltage of 16.0 V (corresponding to a luminance of

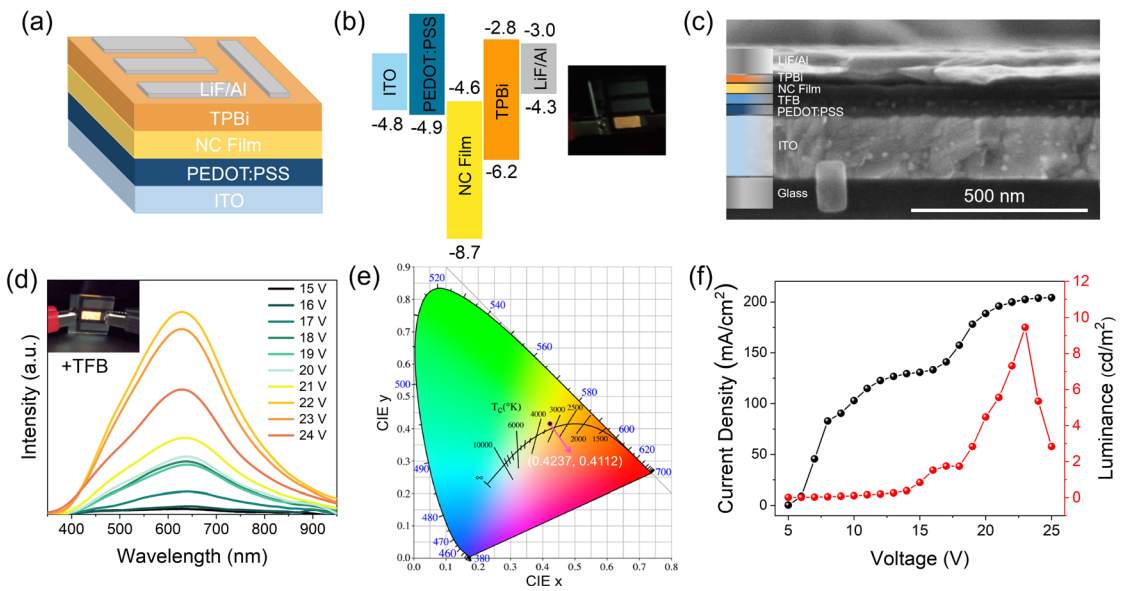

Fig. 5 (a) Device structure and (b) energy band diagram (relative to the vacuum level) of the Sb-doped $CsAgCl_2$ NC LEDs. Inset: photograph of an LED driven by a 14 V bias. (c) Cross-sectional SEM image of a TFB-incorporated device. (d) EL spectra of the resulting LEDs at different applied voltages. Inset: photograph of the LED driven by a 22 V bias. (e) CIE coordinates and (f) *I*–*V*–*L* characteristics of the LED devices.

1 cd m^{-2}) with a maximum luminance up to 9.6 cd m^{-2} and an EQE of 0.02%. We note that such a luminous efficiency is lower than those of 3D $CsAgIn_{0.9}Bi_{0.1}Cl_6$-based LEDs (maximum EQE ~0.08%) and our recently developed MA_2CuCl_3 warm white LEDs (~0.04%),[5,10] which points to the fact that our LEDs still suffer from significant injection barriers and/or charge injection imbalance, partially due to the low carrier mobility of $CsAgCl_2$ because of its 0D crystal structure at the molecular level. In addition to a better device design, we foresee that the EL performance can be further increased by enhancing the PLQY of these $CsAgCl_2$ NCs because the maximum value of the yield currently achievable for NC thin films is only 30%. Great effort will be needed to ensure brighter PL from the NC emitters. To further evaluate the operational stability of the ensuing LEDs, time-dependent EL measurement was performed, without using epoxy or silica encapsulation for protection. It is seen that the EL spectra of the resulting LEDs retain the stable peak position and FWHM after 4 h of continuous operation at 20 V; however, EL intensity gradually decreased over time, which retained ~50% of its initial intensity at $T = 1$ h (Fig. S10, ESI†). As such, a further study is required to clarify the possible degradation pathways and mechanisms, with the aim of improving their operational stability.

Conclusions

We have presented a novel synthetic approach, which enables the formation of nano-sized $CsAgCl_2$ crystals in the colloidal state and thereby enables these fascinating materials to be used in electrically driven warm white LEDs. The successful application of this method for crystallization depends on the use of $EuCl_3$, which was used for the first time as an efficient halide source and to offer a better control over growth kinetics of the $CsAgCl_2$ nanoparticles. Furthermore, we demonstrated a trace doping strategy with Sb^{3+}, which simultaneously improves the PL performance of the $CsAgCl_2$ NCs and reduces their particle size to several nanometers, making them suitable for the fabrication of functional compact thin films for EL applications. Our prototype LEDs fabricated with these Sb-doped $CsAgCl_2$ NCs show favorable warm white-light emission, which represents the first successful demonstration of EL from this kind of pure Ag-based metal halide material. The potential for LED applications along with the low-toxicity properties of these pure Ag-based metal halides will open up a new era of research in the field of Pb-free optoelectronics.

Conflicts of interest

The authors declare no competing financial interest.

Acknowledgements

This work was financially supported by the National Natural Science Foundation of China (no. 22179072 and 22088102), the Natural Science Foundation of Shandong Province (no. ZR2021QF006 and ZR2021QB010), the Outstanding Youth Science Foundation of Shandong Province (overseas) (no. 2022HWYQ-006), and the Qilu Youth Scholar Foundation of Shandong University (no. 62460082163114).

References

1 A. Dey, A. F. Richter, T. Debnath, H. Huang, L. Polavarapu and J. Feldmann, Transfer of Direct to Indirect Bound Excitons by Electron Intervalley Scattering in $Cs_2AgBiBr_6$ Double Perovskite Nanocrystals, *ACS Nano*, 2020, **14**, 5855–5861.

2 J. Huang, T. Lei, M. Siron, Y. Zhang, S. Yu, F. Seeler, A. Dehestani, L. N. Quan, K. Schierle-Arndt and P. Yang, Lead-free Cesium Europium Halide Perovskite Nanocrystals, *Nano Lett.*, 2020, **20**, 3734–3739.

3 T. Cai, W. Shi, S. Hwang, K. Kobbekaduwa, Y. Nagaoka, H. Yang, K. Hills-Kimball, H. Zhu, J. Wang, Z. Wang, Y. Liu, D. Su, J. Gao and O. Chen, Lead-Free $Cs_4CuSb_2Cl_{12}$ Layered Double Perovskite Nanocrystals, *J. Am. Chem. Soc.*, 2020, **142**, 11927–11936.

4 Q. Fan, G. V. Biesold-McGee, J. Ma, Q. Xu, S. Pan, J. Peng and Z. Lin, Lead-Free Halide Perovskite Nanocrystals: Crystal Structures, Synthesis, Stabilities, and Optical Properties, *Angew. Chem., Int. Ed.*, 2020, **59**, 1030–1046.

5 X. Meng, S. Ji, Q. Wang, X. Wang, T. Bai, R. Zhang, B. Yang, Y. Li, Z. Shao, J. Jiang, K.-L. Han and F. Liu, Organic–Inorganic Hybrid Cuprous-Based Metal Halides for Warm White Light-Emitting Diodes, *Adv. Sci.*, 2022, 2203596.

6 M. Liu, Q. Wan, H. Wang, F. Carulli, X. Sun, W. Zheng, L. Kong, Q. Zhang, C. Zhang, Q. Zhang, S. Brovelli and L. Li, Suppression of Temperature Quenching in Perovskite Nanocrystals for Efficient and Thermally Stable Light-Emitting Diodes, *Nat. Photonics*, 2021, **15**, 379–385.

7 J. Zhang, L. Wang, C. Jiang, B. Cheng, T. Chen and J. Yu, CsPbBr3 Nanocrystal Induced Bilateral Interface Modification for Efficient Planar Perovskite Solar Cells, *Adv. Sci.*, 2021, **8**, 2102648.

8 L. Wang, Z. Shi, Z. Ma, D. Yang, F. Zhang, X. Ji, M. Wang, X. Chen, G. Na, S. Chen, D. Wu, Y. Zhang, X. Li, L. Zhang and C. Shan, Colloidal Synthesis of Ternary Copper Halide Nanocrystals for High-Efficiency Deep-Blue Light-Emitting Diodes with a Half-Lifetime above 100 h, *Nano Lett.*, 2020, **20**, 3568–3576.

9 Z. Ma, Z. Shi, D. Yang, F. Zhang, S. Li, L. Wang, D. Wu, Y. Zhang, G. Na, L. Zhang, X. Li, Y. Zhang and C. Shan, Electrically-Driven Violet Light-Emitting Devices Based on Highly Stable Lead-Free Perovskite $Cs_3Sb_2Br_9$ Quantum Dots, *ACS Energy Lett.*, 2020, **5**, 385–394.

10 Y. Zhang, Z. Zhang, W. Yu, Y. He, Z. Chen, L. Xiao, J.-J. Shi, X. Guo, S. Wang and B. Qu, Lead-free Double Perovskite $Cs_2AgIn_{0.9}Bi_{0.1}Cl_6$ Quantum Dots for White Light-Emitting Diodes, *Adv. Sci.*, 2022, **9**, 2102895.

11 D. Wu, J. Zhou, W. Kang, K. An, J. Yang, M. Zhou, P. He, Q. Huang and X. Tang, Ultrastable Lead-Free $CsAgCl_2$

Perovskite Microcrystals for Photocatalytic CO_2 Reduction, *J. Phys. Chem. Lett.*, 2021, **12**, 5110–5114.

12 T. Tian, X. Xiong, Y. Zhao, H. Li, W. Wang and L. Wang, Ultra-Wideband Warm White Light Emission from Self-Trapped Excitons in $CsAgCl_2$, *J. Alloys Compd.*, 2022, **895**, 162632.

13 Y. Bekenstein, J. C. Dahl, J. Huang, W. T. Osowiecki, J. K. Swabeck, E. M. Chan, P. Yang and A. P. Alivisatos, The Making and Breaking of Lead-Free Double Perovskite Nanocrystals of Cesium Silver–Bismuth Halide Compositions, *Nano Lett.*, 2018, **18**, 3502–3508.

14 S. E. Creutz, E. N. Crites, M. C. De Siena and D. R. Gamelin, Colloidal Nanocrystals of Lead-Free Double-Perovskite (Elpasolite) Semiconductors: Synthesis and Anion Exchange To Access New Materials, *Nano Lett.*, 2018, **18**, 1118–1123.

15 J. Shamsi, Z. Dang, P. Ijaz, A. L. Abdelhady, G. Bertoni, I. Moreels and L. Manna, Colloidal CsX (X = Cl, Br, I) Nanocrystals and Their Transformation to $CsPbX_3$ Nanocrystals by Cation Exchange, *Chem. Mater.*, 2018, **30**, 79–83.

16 F. Liu, C. Ding, Y. Zhang, T. Kamisaka, Q. Zhao, J. M. Luther, T. Toyoda, S. Hayase, T. Minemoto, K. Yoshino, B. Zhang, S. Dai, J. Jiang, S. Tao and Q. Shen, GeI_2 Additive for High Optoelectronic Quality $CsPbI_3$ Quantum Dots and Their Application in Photovoltaic Devices, *Chem. Mater.*, 2019, **31**, 798–807.

17 Y. Dong, T. Qiao, D. Kim, D. Parobek, D. Rossi and D. H. Son, Precise Control of Quantum Confinement in Cesium Lead Halide Perovskite Quantum Dots via Thermodynamic Equilibrium, *Nano Lett.*, 2018, **18**, 3716–3722.

18 K. J. Laidler, The Development of the Arrhenius Equation, *J. Chem. Educ.*, 1984, **61**, 494.

19 X. Wang, T. Bai, B. Yang, R. Zhang, D. Zheng, J. Jiang, S. Tao, F. Liu and K.-L. Han, Germanium Halides Serving as Ideal Precursors: Designing a More Effective and Less Toxic Route to High-Optoelectronic-Quality Metal Halide Perovskite Nanocrystals, *Nano Lett.*, 2022, **22**, 636–643.

20 Z. Dang, J. Shamsi, F. Palazon, M. Imran, Q. A. Akkerman, S. Park, G. Bertoni, M. Prato, R. Brescia and L. Manna, In Situ Transmission Electron Microscopy Study of Electron Beam-Induced Transformations in Colloidal Cesium Lead Halide Perovskite Nanocrystals, *ACS Nano*, 2017, **11**, 2124–2132.

21 X.-G. Zhou, C.-Q. Yang, X. Sang, W. Li, L. Wang, Z.-W. Yin, J.-R. Han, Y. Li, X. Ke, Z.-Y. Hu, Y.-B. Cheng and G. Van, Tendeloo, Probing the Electron Beam-Induced Structural Evolution of Halide Perovskite Thin Films by Scanning Transmission Electron Microscopy, *J. Phys. Chem. C*, 2021, **125**, 10786–10794.

22 W. Liu, J. Zheng, M. Shang, Z. Fang, K.-C. Chou, W. Yang, X. Hou and T. Wu, Electron-beam irradiation-hard metal-halide perovskite nanocrystals, *J. Mater. Chem. A*, 2019, **7**, 10912–10917.

23 S. Levy, S. Khalfin, N. G. Pavlopoulos, Y. Kauffmann, G. Atiya, S. Shaek, S. Dror, R. Shechter and Y. Bekenstein, The Role Silver Nanoparticles Plays in Silver-Based Double-Perovskite Nanocrystals, *Chem. Mater.*, 2021, **33**, 2370–2377.

24 F. Liu, C. Ding, Y. Zhang, T. S. Ripolles, T. Kamisaka, T. Toyoda, S. Hayase, T. Minemoto, K. Yoshino, S. Dai, M. Yanagida, H. Noguchi and Q. Shen, Colloidal Synthesis of Air-Stable Alloyed $CsSn_{1-x}Pb_xI_3$ Perovskite Nanocrystals for Use in Solar Cells, *J. Am. Chem. Soc.*, 2017, **139**, 16708–16719.

25 B. Yang, X. Mao, F. Hong, W. Meng, Y. Tang, X. Xia, S. Yang, W. Deng and K. Han, Lead-Free Direct Band Gap Double-Perovskite Nanocrystals with Bright Dual-Color Emission, *J. Am. Chem. Soc.*, 2018, **140**, 17001–17006.

26 J. Luo, X. Wang, S. Li, J. Liu, Y. Guo, G. Niu, L. Yao, Y. Fu, L. Gao, Q. Dong, C. Zhao, M. Leng, F. Ma, W. Liang, L. Wang, S. Jin, J. Han, L. Zhang, J. Etheridge, J. Wang, Y. Yan, E. H. Sargent and J. Tang, Efficient and Stable Emission of Warm-White Light from Lead-Free Halide Double Perovskites, *Nature*, 2018, **563**, 541–545.

27 Z. Li, G. Song, Y. Li, L. Wang, T. Zhou, Z. Lin and R.-J. Xie, Realizing Tunable White Light Emission in Lead-Free Indium(III) Bromine Hybrid Single Crystals through Antimony(III) Cation Doping, *J. Phys. Chem. Lett.*, 2020, **11**, 10164–10172.

28 S. Li, J. Luo, J. Liu and J. Tang, Self-Trapped Excitons in All-Inorganic Halide Perovskites: Fundamentals, Status, and Potential Applications, *J. Phys. Chem. Lett.*, 2019, **10**, 1999–2007.

29 A. Cabot, M. Ibáñez, P. Guardia and A. P. Alivisatos, Reaction Regimes on the Synthesis of Hollow Particles by the Kirkendall Effect, *J. Am. Chem. Soc.*, 2009, **131**, 11326–11328.

30 G. Li, F. W. R. Rivarola, N. J. L. K. Davis, S. Bai, T. C. Jellicoe, F. de la Peña, S. Hou, C. Ducati, F. Gao, R. H. Friend, N. C. Greenham and Z.-K. Tan, Highly Efficient Perovskite Nanocrystal Light-Emitting Diodes Enabled by a Universal Crosslinking Method, *Adv. Mater.*, 2016, **28**, 3528–3534.

31 H. Shen, Q. Gao, Y. Zhang, Y. Lin, Q. Lin, Z. Li, L. Chen, Z. Zeng, X. Li and Y. Jia, Visible Quantum Dot Light-Emitting Diodes with Simultaneous High Brightness and Efficiency, *Nat. Photonics*, 2019, **13**, 192–197.

32 C. Yi, C. Liu, K. Wen, X.-K. Liu, H. Zhang, Y. Yu, N. Fan, F. Ji, C. Kuang and B. Ma, Intermediate-Phase-Assisted Low-Temperature Formation of γ-$CsPbI_3$ Films for High-Efficiency Deep-Red Light-Emitting Devices, *Nat. Commun.*, 2020, **11**, 1–8.